SANDIA REPORT

SAND2004-5391
Unlimited Release
Printed October 2004

Material Characterization for Inertia Welding Development Progress Report: Part I

Microstructural Characteristics and Phase Transformation of 21-6-9 Inertia Welds Produced at Sandia National Laboratories, California

N. Yang, M. Balmforth, S. Robinson, C. San Marchi, T. Headley

Approved for public release; further dissemination unlimited.

Sandia National Laboratories

TOTAL PAGES: 40
COPY

ELECTRONIC

Issued by Sandia National Laboratories, operated for the United States Department of Energy by Sandia Corporation.

Material Characterization for Inertia Welding Development Progress Report: Part I

Microstructural Characteristics and Phase Transformation of 21-6-9 Inertia Welds Produced at Sandia National Laboratories, California

Nancy Yang
Analytical Materials Science

Mikal Balmforth and Steven Robinson
GTS & H-Gear Engineering

Christopher San Marchi
Engineered Materials

Thomas Headley
Materials Characterization

Sandia National Laboratories, California
P.O. Box 969 – MS 9403
Livermore, CA 94551-0969

Abstract

Inertia welding (IW), a solid-state process, is being considered for fabricating GTS-related components. Our programmatic objective is to gain better insight into the physical and chemical metallurgy of inertia welded joints. In addition, we are studying how the metallurgy is influenced by the process variables and subsequently affecting the weld performance. Three welds of 21-6-9 alloys were produced at SNL, CA for the current investigations. To achieve our scientific objectives, we have conducted extensive characterization concerning microstructural evolution and phase transformation of the welds. The preliminary findings are discussed and presented in this progress report.

Two major metallurgical characteristics in the current IW welds identified are recrystallization and δ- ferrite transformation. A major portion of the weld has undergone recrystallization during welding. The recrystallization resulted in moderate softening in the weld affected zone (WAZ). The hardness of the WAZ was on average, about 20% lower than that of the base alloy. The degree of nucleation and grain growth varied nonlinearly across the weld, which resulted in W-shaped hardness profiles reaching the maximum at the interface. The δ-ferrite transformation was highly localized, taking place primarily at the weld interface, and was decorated along grain boundaries of the newly recrystallized fine-grained austenite matrix.

Cause of nonlinear recrystallization and δ-ferrite transformation may be related to combine factors of thermal heating and plastic deformation unique to solid-state welding. Grain refinement at the interface is suspected to be a result of high number of nucleation sites supplied from dense dislocation network. Grain coarsening next to the interface layer could be a result of fewer nucleation sites due to lower dislocation density at relatively long distance from the plastically deformed weld interface. δ-ferrite-austenite phase transformation mechanism and kinetics is unclear and is currently being investigated.

In short, the combined factors of plastic deformation and thermal heating during inertia welding may be responsible for the resultant recrystallization and δ-ferrite transformation in the inertia joints. Other possible factor(s), e.g., banded macrosegregation of the forged alloy precursors are also being examined.

CONTENTS

FIGURES

TABLES

Introduction

Welding is a crucial procedure for fabricating DP components. Solidification welding processes such as Gas Tungsten Arc welding (GTAW) and electron beam welding (EBW) have been used for decades for welding of GTS parts. Because of their long history, the metallurgy of GTAW and EBW has been studied extensively and is relatively well understood (Ref. 1,2). However, fusion welding processes, such as these, require control of a large number of processing parameters and typically result in joints that have degraded mechanical properties compared to the base materials. Presently, inertia welding (IW) is being considered as a viable process for GTS applications. In principle, inertia welding requires control of only three processing parameters: speed at which the part is turned, the axial force with which the parts are brought together, and the inertia applied to the system. In addition, the materials remain in the solid state during processing, thus eliminating the problems associated with solidification, such as microsegregation and hot cracking. At SNL, because of short programmatic history, IW metallurgy and its correlation to engineering performance for GTS applications are less well understood. This project is one of several DP funded technical tasks to study IW technology in SNL. A main focus of the current task is to gain insight into microstructural characteristics unique to IW. In addition, we are studying the correlation between process variables and the resulting microstructures to assess the metallurgical performance for GTS applications. The task has placed a special interest on phase transformation of austenite to δ-ferrite, which is known to impact the hydrogen compatibility of stainless steel alloys. In addition, the evolution of microstructural features induced by the inertia welding was also examined.

This report presents technical progress and preliminary experimental observations for inertia joints produced at SNL, CA. The evolution of microstructure, microhardness, ferrite/austenite morphology and their distribution in the WAZ are discussed.

Intentionally Left Blank

Experiments

Materials

i) Base material

The welded parts were fabricated from 21-6-9 stainless steel forgings. The forgings were made at Precision Metal Products, Inc. in El Cajon, California using material supplied by the Kansas City Plant. The bars were forged into right-circular cylinders, 3.5 in. tall by 3 in. diameter. The nominal composition of the forgings is 19.4 wt% chromium, 6.6 wt% nickel and 9.1 wt% manganese (average of MCN112864 and 112866).

ii) Inertia welded parts

Schematic and design of the inertia weld test parts are shown in Figure 1a-b. The test specimens were made by the staff in Department 8243 and 8225 at SNL, CA using an MTI model 180 inertia welding machine (Figure 1c). There are three main variables in inertia welding. They are, the speed at which the part is turned, the axial force with which the parts are brought together, and the inertia, which is varied by adding or removing flywheels. These variables are combined to produce different amounts of displacement, or upset, as the parts are brought together and the weld is created. The sample identification and welding conditions of the specimens being investigated are shown in Table 1.

Table 1. Test specimen welding conditions.

Sample ID	Speed (RPM)	Force (lbs.)	Inertia (wk^2)	Upset (in.)
Tab 7A	5000	50,000	8.344	.021
Tab 8C	6000	40,000	8.344	.028
Tab 8E	5000	60,000	8.344	.036

a)

2 inches

1.6 in.

2.4 in.

b)

c)
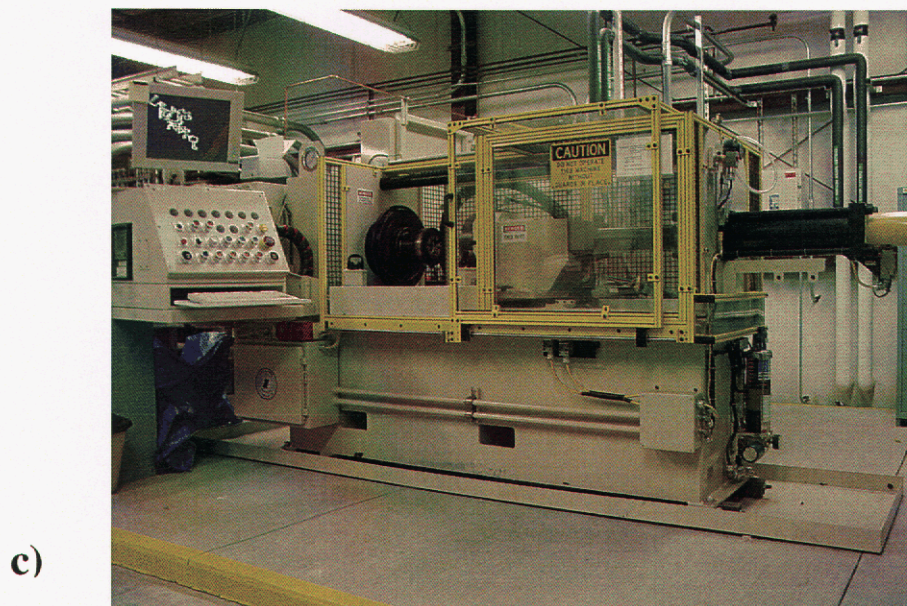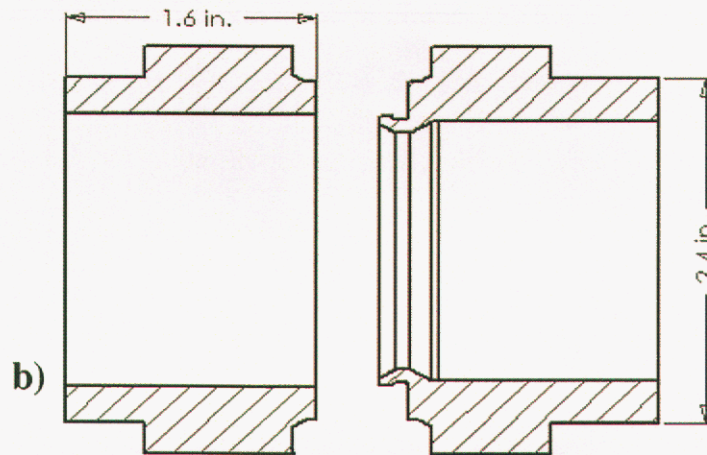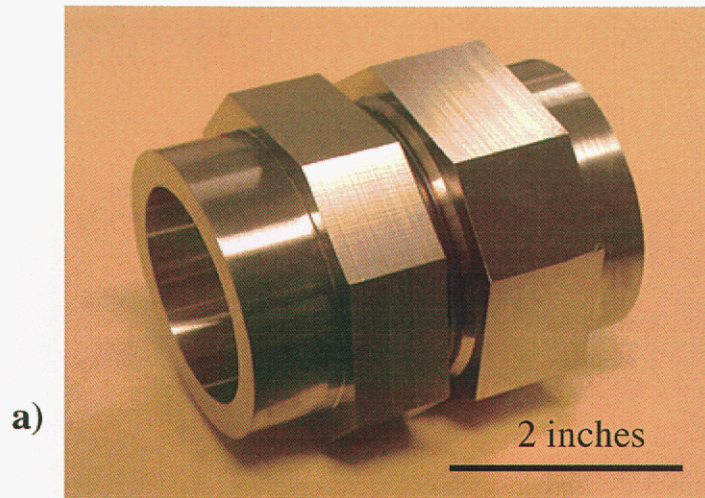
Figure 1: Test sample, a) inertia welded test part, b) schematic of the test part prior to welding, c) MTI model 180 inertia welding machine at SNL/CA.

Experimental Procedures

i) Diagnostic approaches
The techniques used for characterizing the inertia welds include: optical metallographic (OM) analyses, scanning electron microscopy (SEM), electron probe microanalysis (EPMA), transmission electron microscopy (TEM), electron backscattered diffraction (EBSD) and Vickers microhardness indentation.

ii) Equipment used
The optical microscope used is Leitz orthoplan equipped with image analysis software.

SEMs used are JEOL 5910, JEOL 840 and JEOL6400F and JEOL 6700F made by JEOL, USA, MA. All SEMs are equipped with backscattered electron imaging (BEI) detector and energy dispersive x-ray spectrometer (EDS) made either by Oxford Instruments America, MA or Thermo Electron Co. WI. In addition, both the JEOL 6400F and 6700F SEMs are also equipped with electron backscattered diffraction pattern (EBSP) packages made by Oxford Instruments, MA.

Electron microprobe used is JEOL 8200 Super probe, equipped with five automated wavelength dispersive x-ray (WDS) spectrometers and an EDS, made by Thermo Electron Co. WI. The transmission electron microscope used was a Philips CM30 equipped with EDS made by Thermo Electron, WI, and electron energy loss spectrometer (EELS) with advanced Gatan Imaging Filtering software (GIF).

The Vickers microhardness testers used are Model 99-40065 and Micromet 5104 made by Buehler Ltd. Illinois.

Sample preparation

i) Bulk specimen for SEM, EMPA and Vickers indentation analyses
Specimens for microstructure, chemical composition, texture and microhardness examinations were prepared using standard metallographic mounting and polishing process as described below.

Step 1: Longitudinal cross sections of the welded forgings were sliced from the welded parts as shown in the following schematic.
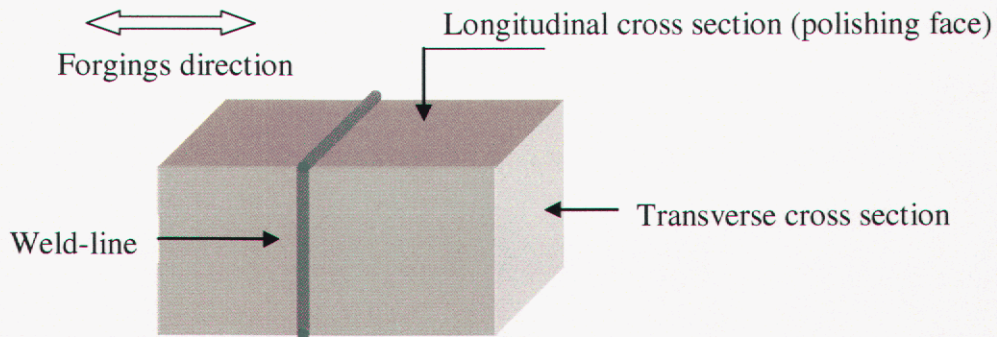
Step 2: The cross-section surfaces were ground and polished using standard metallographic techniques:

1. Samples were planed with 9µm diamond compound and alcohol lubricant.
2. One minute of grinding with 6µm diamond compound and alcohol lubricant.
3. One minute of grind with 3µm diamond compound and alcohol lubricant.
4. Polished for 30 seconds with equal parts of colloidal alumina and colloidal silica at 150Newton (Nt). During the last 10 seconds of polish, lap cloth is flushed with de-mineralized water.
5. If scratches persist after Step 4, sample is polished for one minute at <40Nt with 200ml colloidal silica and 5 drops each of Ammonium Hydroxide, Hydrogen Peroxide, and Keller's Etch. During the last 10 seconds of polish, lap cloth is flushed with de-mineralized water.
6. Polished samples are cleaned ultrasonically in a soapy detergent solution, rinsed with Isopropyl and warm air-dried.

ii) Thin film specimen for TEM and in-situ hot stage TEM analyses

Slices ~1 mm thick were cut transverse to the weld plane on a slow-speed diamond saw, ground on SiC paper to ~125 µm thick, and lightly etched to reveal the weld interface.
3 mm diameter disks were punched with their centers at or near the weld interface, and were electropolished in 5% perchloric acid in methanol at 40V dc and –50C. Some disks were subsequently Ar+ ion-milled to extend the thin area closer to or into the weld interface layer. Samples were also prepared from the base metal at a distance many mm from the weld interface by this electropolishing procedure.

Experimental procedures

i) Macroscopic structure of the welds

Weld integrity and landscape of weld affected zone (WAZ) were examined using optical and SEM/BEI imaging of oxalic-etched and as-received unetched welds respectively.

ii) Microstructure of δ-ferrite and austenite matrix

Microstructure of the overall weld and δ-ferrites and austenite matrix were examined either using SEM with BEI/SEI or TEM imaging depending on the resolution requirement. For submicron-scale microstructure features, TEM with bright field and dark field (TEM/BF/DF) imaging were employed.

iii) Grain size measurement

Grain size of ferrite and austenite matrix was estimated by intercept method using SEM/BEI images. Average grain size is the average grain boundary spacing measured along 200um length of intercepting line.

iv) Texture and phase identity

Texture or preferred orientation of ferrite and austenite in the welds and base alloys were characterized using crystallographic information provided by TEM with selected area electron diffraction patterns (TEM/SADP) and SEM/EBSP maps. SEM/EBSP is a technique provides crystal structure and crystal orientation of phase(s) and/or grains in the region of interest as illustrated in Figure 2a-f. Texture (or preferred orientation) is determined based on statistical fraction of each orientation within an orientation map (Fig 2d-f). The EBSP system also has built-in software for differentiating phase(s) of different crystal structure using a binary map. The binary map is very effective to discern body centered cubic (bcc) ferrite from face center cubic (fcc) austenite matrix and compute their volume fractions. There is an additional EBSP software feature, referred as quality map, which is served as an indicator for quality of EBSP patterns in the local areas. Low grayscale in the map means poor EBSP pattern quality implying presence of lattice distortion or imperfection. The lattice distortion may come from variety sources such as strain field, defect, grain boundary and/or surface artifact. A quality map often provides clearly visual definition of grain boundaries, which do not possess crystal structure of its own and therefore revealed as dark line (Fig. 13b). In general, the technique is most effective for the feature size greater than 2-3 um.

```
Key            Phase              area %     Detail

Black          Not Solved          2.3       Unsolved points
Yellow         Iron (Alpha)       10.5       Cubic, BODY
Magenta        Iron (Gamma)       87.3       Cubic, FACE

Site area: 285.405 um2
EBSD pixel size: 0.025 um2
```
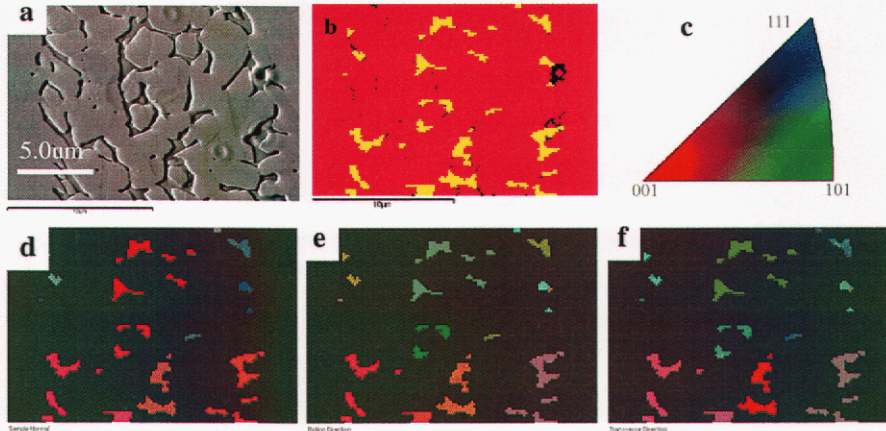

Figure 2: Illustration of EBSP mapping, a) SEM/SEI image of the chemical etched area of interest, b) Binary maps show ferrite phase (yellow) and austenite (pink), c) Color code for ferrite orientation, d-f) ferrite orientation maps along three axes, sample normal, transverse and rolling directions (Inertia direction). Note: table shows area% and pixel counting statistic.

v) Elemental composition and chemical segregation

Chemical composition of a features and their variation were quantified using EMPA/WDS analyses. For the small microstructural features where quantification was not feasible, qualitative elemental X-ray mapping and TEM/EDS were employed instead. Average forging composition was computed from WDS measurements across the sampling area. In general, instrumental error for WDS and EDS analyses is about $\pm$ 3-5% and ±10 % of the actual composition respectively. Detection limits are ≥ 0.1wt% and ≥ 0.5 wt% for WDS and EDS respectively.

vi) Microhardness

Hardness was measured using Vickers indentation method at a 25 g-load. Vickers hardness number (VHN) is computed based on size of diamond indent relative to certified standard materials.

Experimental Results

Landscape of IW welds and weld integrity

Landscape of welds was studied using optical imaging of chemical etched weld cross sections. Comparison of landscapes between the current inertia welds (IW) and a typical fusion welded electron beam weld (EBW) are shown in Figure 3a-b. The images illustrate a fundamental difference between a solid-state welded IW and fusion-welded EBW. For instance, IW contains a narrow layer of mechanical-induced metal flow patterns, <2.0 mm while EBW contains a wide region of solidified dendrites, >3.0 mm (Fig. 4a-b). There are additional landscape features in the current inertia welds, i.e. flash trap on the outer diameter (OD) and upset on the inside diameter (ID) (Fig. 3a). Metallurgical issues related to flash trap and upset are beyond the scope of this study.
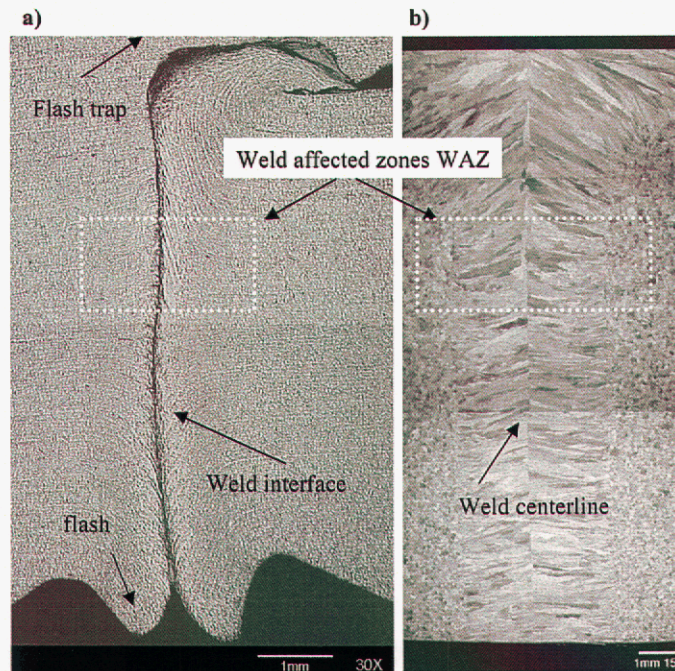
Figure 3: Landscape of welds shown by optical imaging a) Inertia weld (IW), b) Electron beam weld (EBW), The amount of flash is closely related to the upset measured. Note: there are major difference in landscape between solid-state weld and fusion-weld.
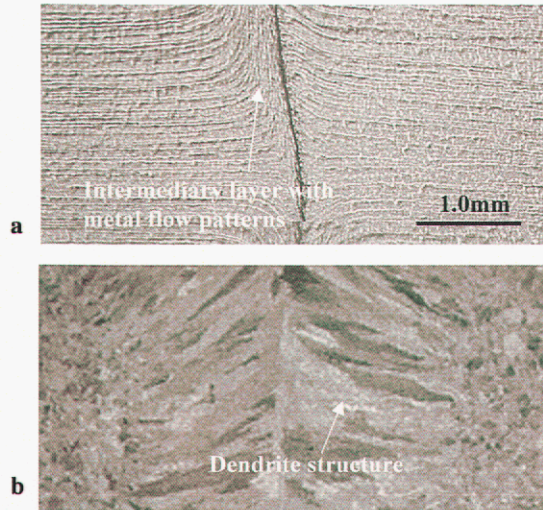
Figure 4: Weld landscape shown by optical images at higher magnification, a) Metal flow patterns of IW, b) Dendrite structure of EBW

High magnification optical imaging shows the IW weld affected zone (WAZ) contained several layered features of different metal flow characteristics (Fig. 5). In addition to a thin layer weld interface, there is a ~400um wide layer, referred as "intermediary layer", between the weld interface and as-forged base alloy. These layered features are more or less symmetrical on both sides across the weld interface. The IW joints generally were well bonded along the length of interest.
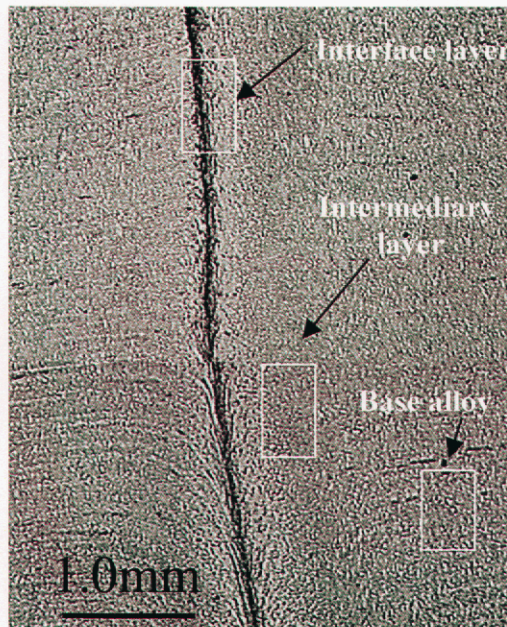
Figure 5: Layers in the WAZ separated by different metal flow pattern

General grain structure and alloy composition uniformity

Grain structure of the various layered features across the WAZ was investigated further utilizing optical and SEM/BEI images. A typical grain structure composite across the weld is shown in Figure 6a-c, which is a good representation of all welds investigated.

The grain structure, and grain size in particular, is non-uniform across the WAZ. BEI imaging shows the weld-interface is a layer with a finite width, ~200um, contain extremely fine features, barely visible in the following images (Fig. 6b-c). The intermediary layer, ~400 um wide next to the interface layer, consisted of much coarser grains which are visible in both optical and BEI images (Fig 6b-c).
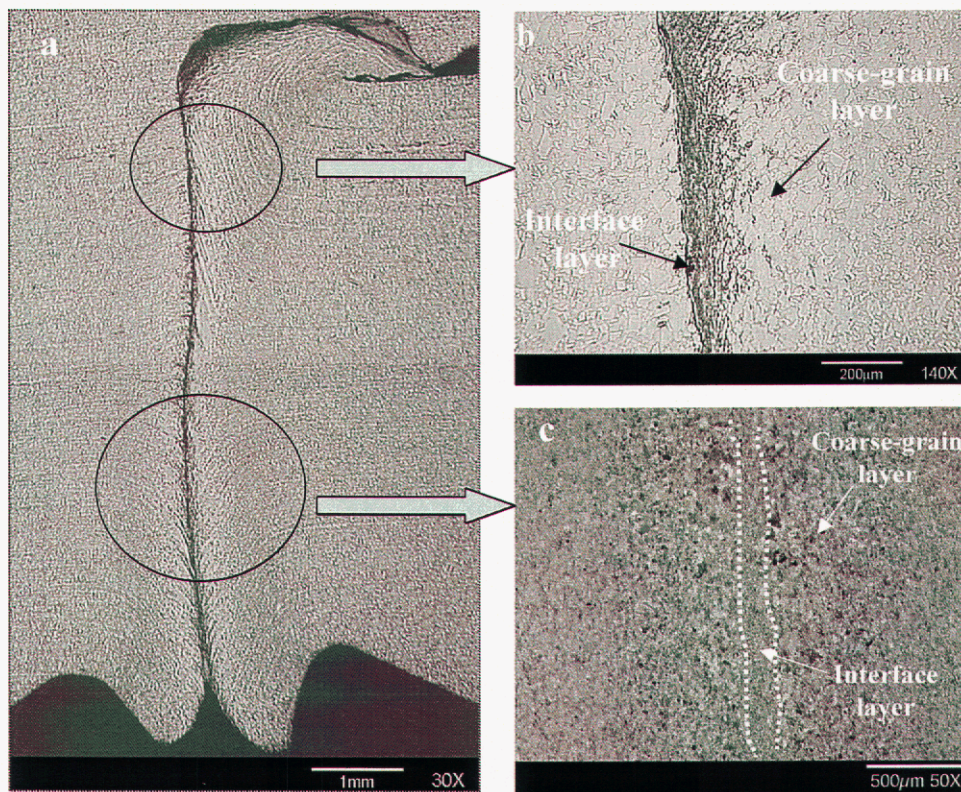
Figure 6: Layered features in the WAZ revealed by optical and SEM/BEI images for weld Tab7A a) Overall landscape by optical image (chemical etched), b) Coarse-grained and interface layers by optical image (chemical etched), c) Interface layer and coarse-grained layers by SEM/BEI (as-polished)

Variation of grain size across the weld was interrogated further using SEM/BEI images at higher magnification as shown in Figure 7. The BEI image shows the interface layer actually contained a bimodal grain structure of different grain sizes, ≤3.0 um and ≥8.0 um (Fig. 7a). The fine grains tend to cluster into strands or layers. The fine-grained layers in the interface layer were commonly seen in other weld, IW8C2, near the flash trap area (Fig. 8a-c). Grains in the intermediary layer are much coarser with average grain size of ~8.0 um. There are large numbers of anomalous large grains >>20um, in the intermediary layer. The large grains usually were located along the boundary with the interface layer (Fig 6c &7b). However, there are still minor amounts of fine-grained remnants in this intermediary layer (Fig 7b).

Average grain size across the WAZ was estimated from the BEI images shown in Figure 7a-d. A plot of grain size with distance shows a nonlinear profile across the WAZ, reaching a peak at the intermediary layer, ~200-300 um from the interface, Fig. 7(e). Beyond 400um distance, the grain size decreased gradually toward the medium grain size of the base alloy. This nonlinear trend is consistent with those seen and described earlier in Figure 6.

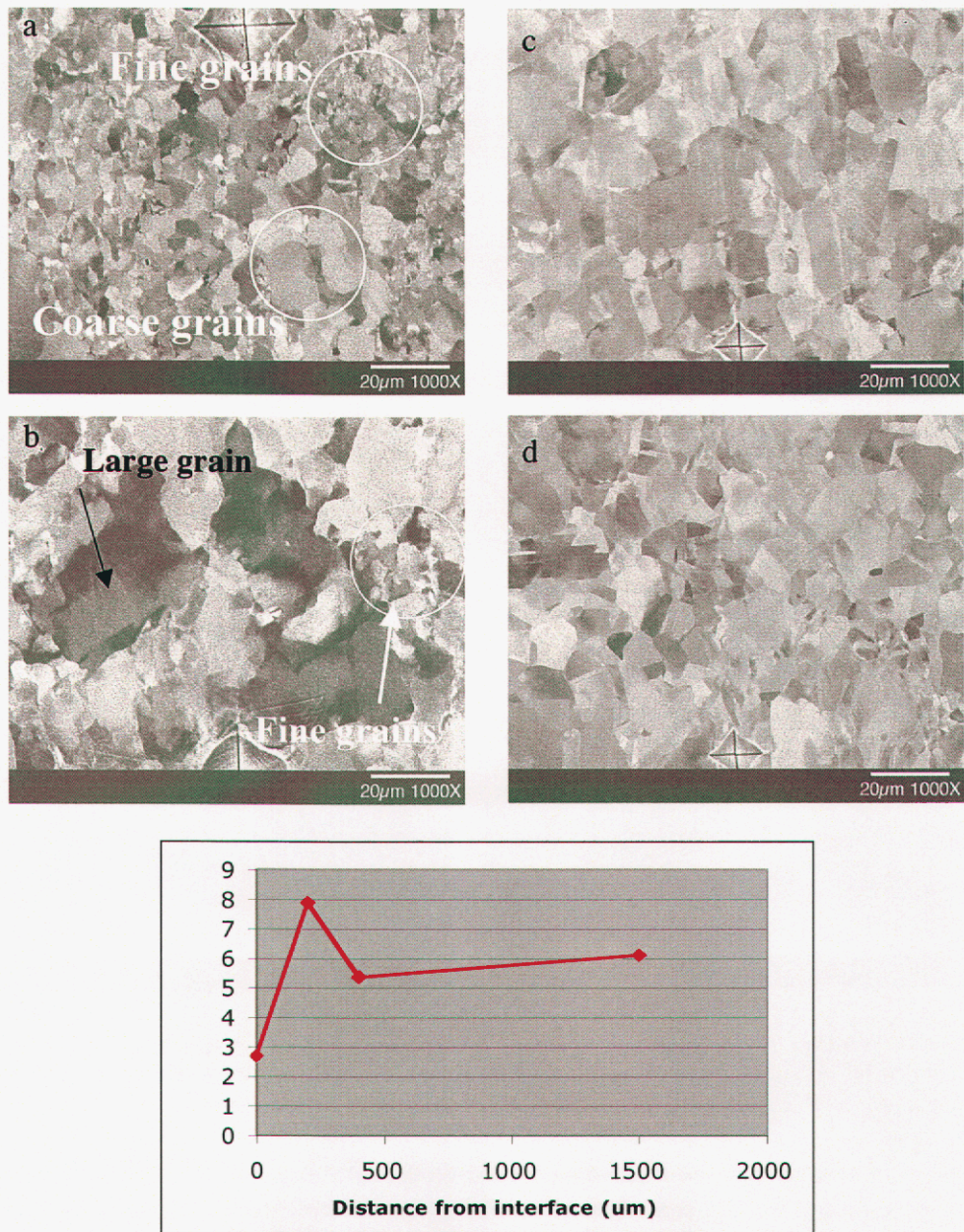Figure 7: Microstructure of austenitic matrix across WAZ, a) Interface layer-bimodal grain structure, b) Intermediary layer - large grains plus few fine grains, c) 600um from interface- uniform medium size grains, d) Base alloy, 1.5mm from interface-uniform medium size grains, e) Average grain size variation across the WAZ. The variation is nonlinear and size peaked at 200-300 um form the interface.

δ-Ferrite phase in the weld was not obvious in these SEM/BEI images. Part of the difficulty may be due to artifacts arising from limitations of BEI resolution and contrast grayscale for small particles. Unfortunately, SEM/BEI contrast of δ-ferrite particles usually appears dark and resembling strongly diffracting austenite matrix grains and/or grooved grain boundaries. To verify presence of δ-ferrite phase and study its microstructure, advanced TEM and EBSP analyses are required and were conducted. These results are discussed subsequently in this report.

Chemical variation near the weld interface was examined using qualitative WDS X-ray mapping. The CrKα X-ray map of the bending tested weld, Tab8C, shows a low level Cr-segregation within the interface layer. Cr-enrichment was observed at the fine-grained strands but absent in the coarse-grained areas within the interface layer (Fig. 8c-d). Quantitative WDS assessment of Cr-segregation is not being conducted for these small Cr-rich features <<3um.

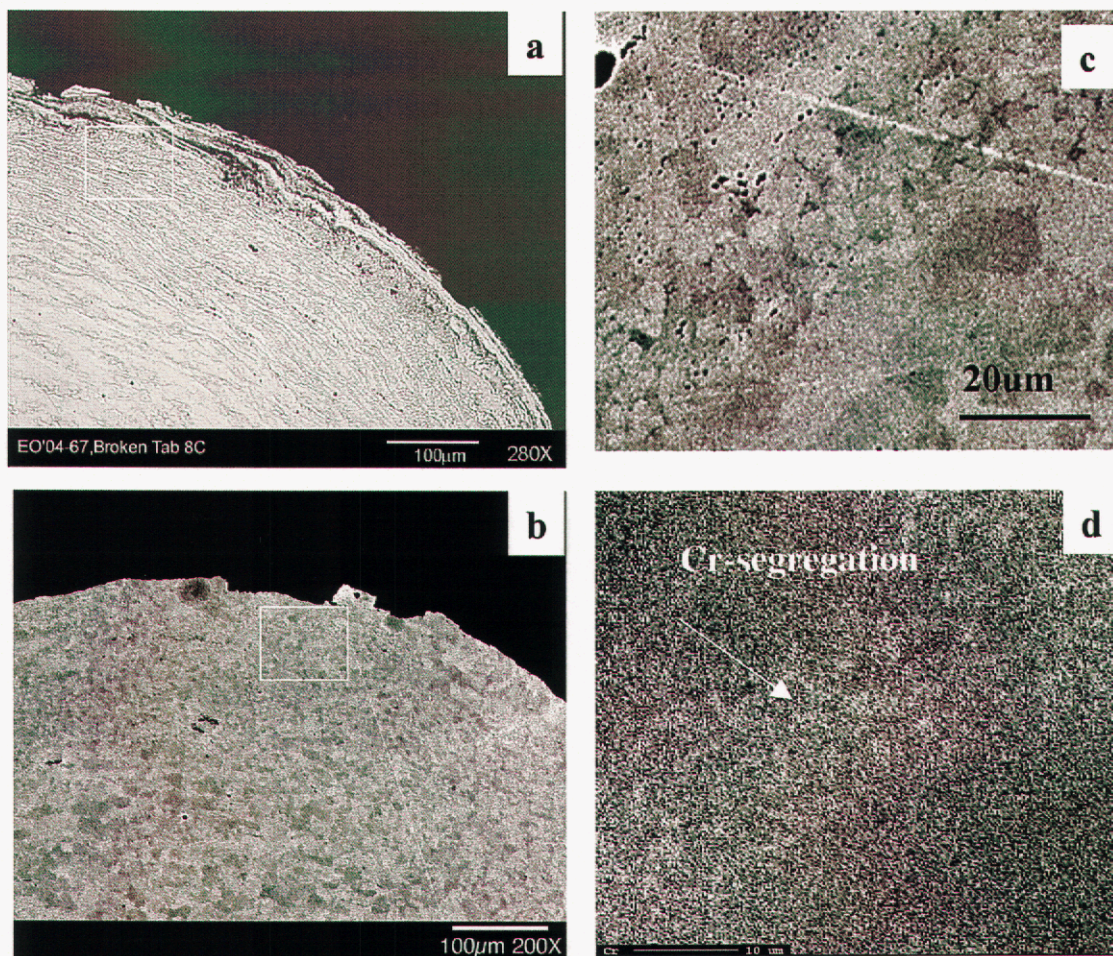Figure 8: a) optical image showing metal flow patterns at the interface layers near
T he fractured flash trap, b) SEM/BEI image of the area in 8a showing fine austenite grains at the interface, c) SEM/BEI image showing fine-grained layers in the interface layer, d) Cr Kα X-ray map of the area in 8c showing Cr-segregation in fine-grained layer. Note: marked box in a) and b) are the fine-grained area in 8c.

Hardness and grain size variation across weld affected zone (WAZ)

Vickers microhardness measurement is a convenient and simple technique for estimating relative local mechanical strength of small and complex welded parts. We have measured hardness at different locations across the weld. Typical Vickers hardness of the current welds ranged from 240-290 VHN and varied with distance relative to the weld-interface. The average hardness of the overall weld is about 20% lower than their forging precursors which possess Vickers hardness of ~300VHN. Plots of hardness with distance exhibited a common W-shaped profile (Fig. 9) is similar to those seen in the Ni-based superalloy by others (Ref. 2). The peaked and minimum hardness in the WAZ is located at the interface and the intermediary layer, ~200-400 um, respectively, on each side of the jointing. Difference in hardness from the peak to the valley of the W-profile is about 10-15% (~30VHN) of the average weld hardness, ~260VHN.
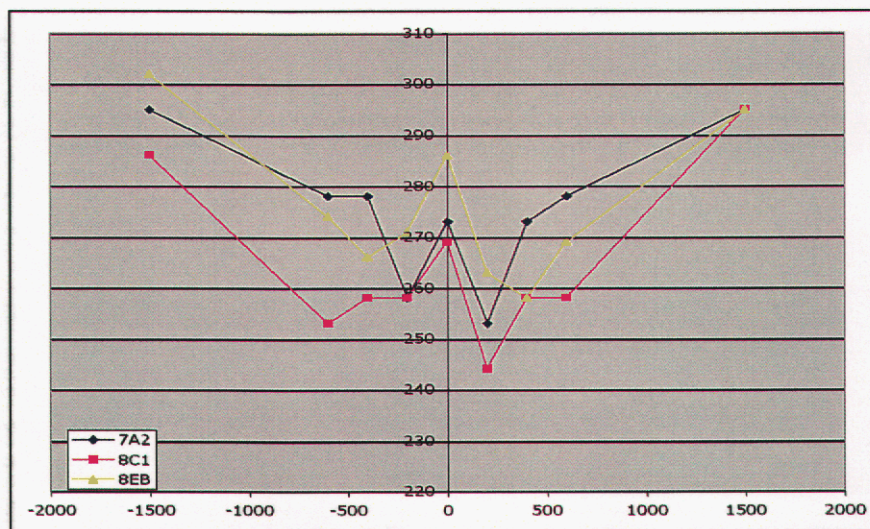

Figure 9: W-shaped hardness profiles across the WAZ.
Note: In the WAZ, hardness peaked at the interface.

20

Correlation between the hardness and grain size across WAZ is qualitatively illustrated in Figure 10. There is an inversed relationship between hardness and grain size (or microstructure feature size). This inversion pointed to the significance of how microstructural feature size influences resultant hardness of the weld.
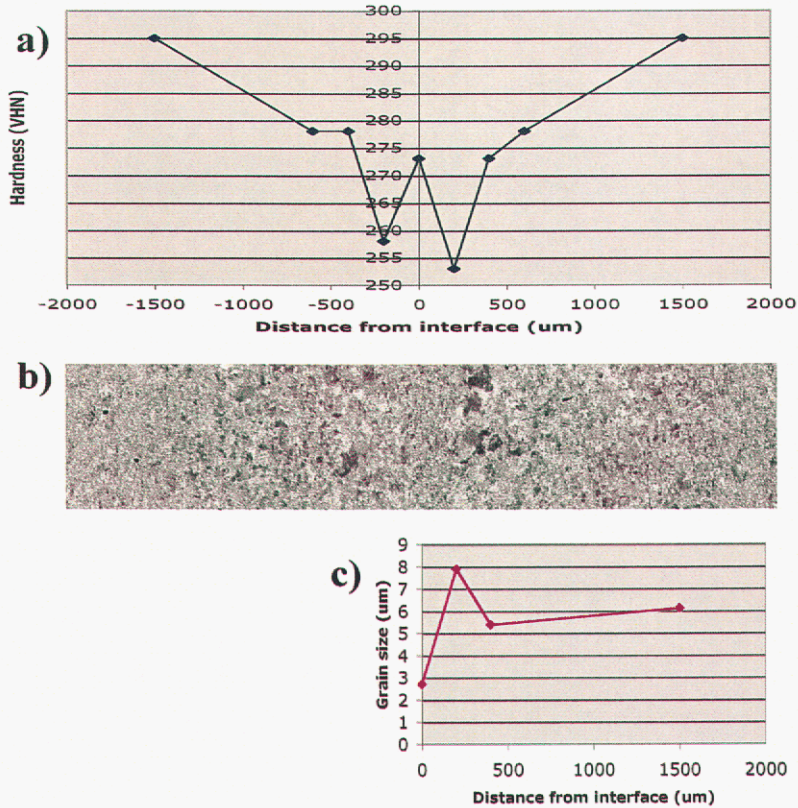
Figure 10: Correlation between grain size and Vickers hardness across the weld, a) Vickers hardness vs. distance for the area in 10b, b) SEM/BEI image of the area of interest, c) Grain size vs. distance of the area in 10b. Note: Inversion between the grain size and hardness profiles. The maximum at 200-400um corresponds to minimum hardness.

IW welding induced microstructure and δ-ferrite transformation

Microstructure of austenite matrix and δ-ferrite induced from the IW welding were studied using complementary techniques, SEM/EBSP mapping and TEM/BF imaging. EBSP mapping carries crystallographic information, which allows us to separate between bcc δ-ferrite and the fcc austenite matrix and their preferred crystal orientations. TEM/BF imaging provides submicron scale information of microstructure features, such as particle morphology, lattice defects, and/or dislocation structure.

SEM/EBSP analyses of texture and δ-ferrite transformation

i) Base alloy

Binary and orientation EBSP maps show the current forged base alloy contained minimal amount of δ-ferrite in the seemingly random oriented austenitic matrix (Figure 11a-d). It is noted that color contrast in many austenite grains was non-uniform. This color contrast variation implied presence of lattice distortion and/or highly strained subgrains which are characteristics of forged metals (Fig.11b)
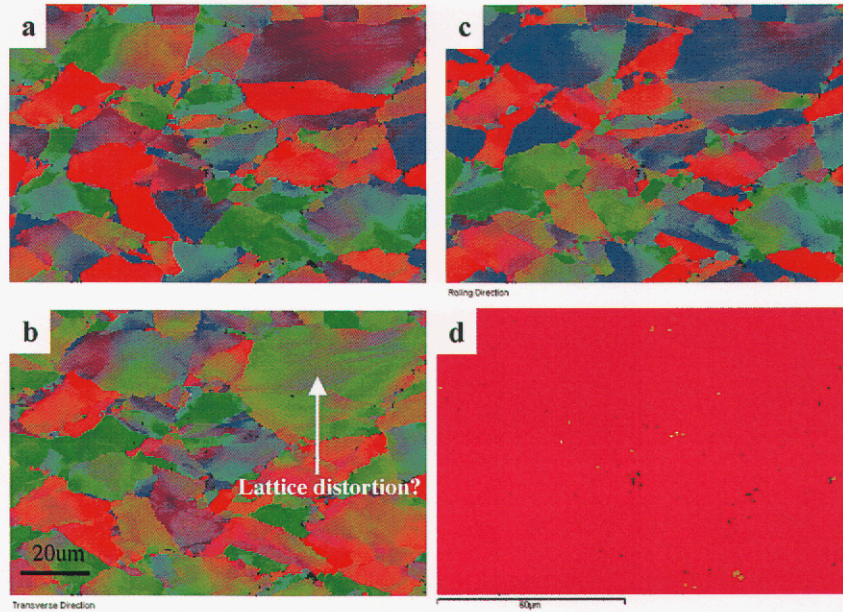
Figure 11: EBSP maps of forged base alloy. a) sample normal direction, b) Transverse direction, c) Rolling direction d) Binary EBSP maps showing minimal amounts of ferrite (yellow) present in the austenite matrix (pink). Note: The non-uniform color contrast of the austenite grains implies lattice distortion induced by mechanical deformation.

ii) Interface layer

Binary EBSP map shows δ-ferrite phase present in the IW welds mainly located along the weld-interface layer (Fig. 12a-b). High magnification binary EBSP maps show small size ferrite phase present along grain boundaries of fine austenite matrix (Fig. 13a-d & 14a-b). There are minimal amounts of ferrite detected in the coarse-grained region within the weld-interface layer.
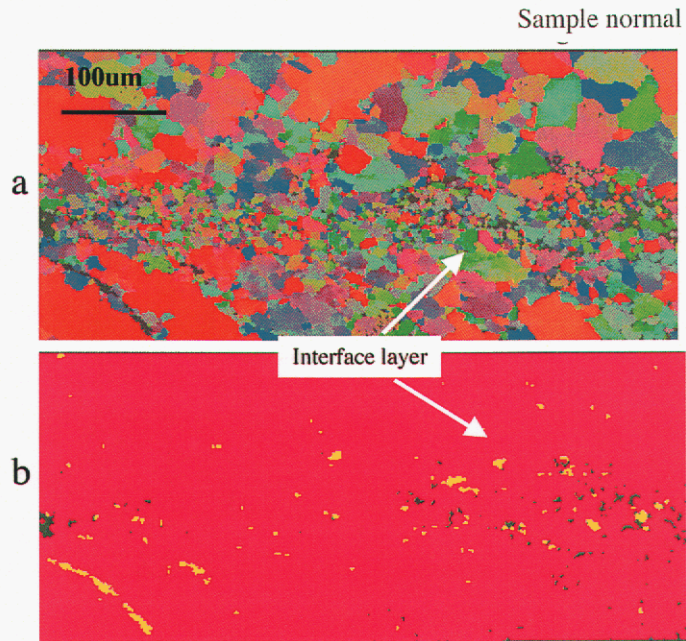
Figure 12: EBSP maps of WAZ, a) austenite orientation map, b) binary map showing δ-ferrite (yellow) present in the austenite matrix (pink).

Regarding texture, all the preliminary EBSP results indicated random crystal orientation distribution of both austenite matrix (Fig 11-13) and δ-ferrite (Fig. 14). It could be possible that fine-scale localized texture may exist in a small area of 20-30um. However, the texture of such small area may be hard to verify by EBSP mapping of two-dimensional planar interceptions. Detailed study of texture in the inertia welds is beyond the scope of this study and should be examined further in a separate milestone.
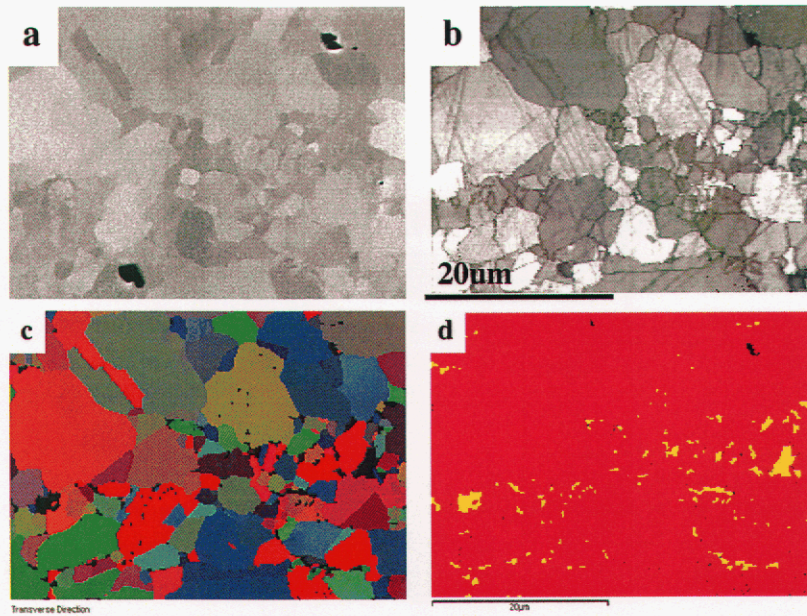
Figure 13: EBSP map showing presence of ferrite along fine-grained boundaries in the interface layer. a) BEI image of the area of interest, b) EBSP quality map defining grain boundaries) of the area in 13a, c) EBSP orientation map of austenite; d) binary EBSP map showing austenite (pink) and ferrite (yellow).
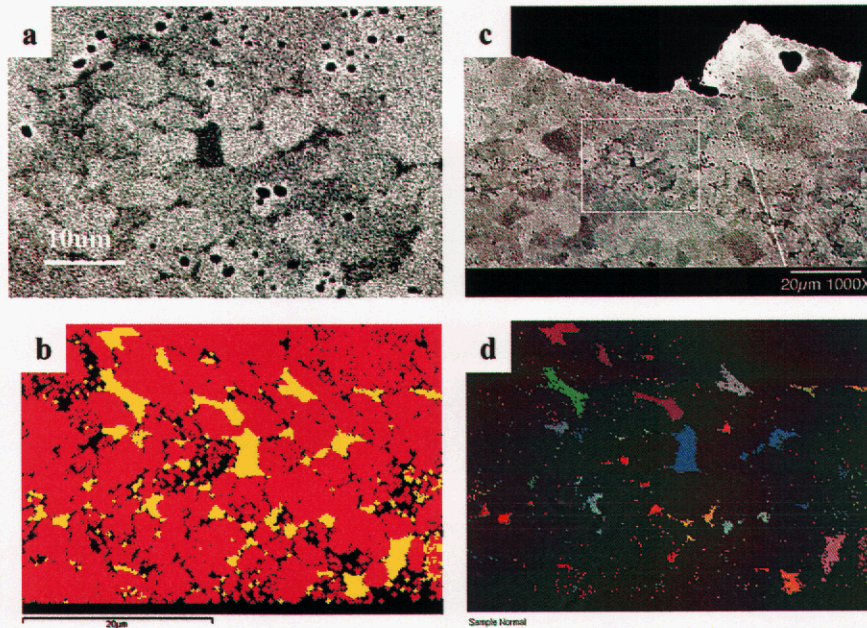
Figure 14: SEM/BEI and corresponding EBSP maps showing ferrite present along austenite grain boundaries, a) SEM/BEI image, b) Binary map of the area shown in 14a, c) SEM/BEI showing the fine-grained austenite layer in the interface layer, d) EBSP orientation map showing random orientation of ferrite particles. Note: the light box in 14c is the area of 14a at lower magnification. Note, dark spots in 14a are Mn-oxides, which is an issue beyond the scope of this report.

24

TEM studies of microstructure and δ-ferrite transformation

Microstructure and δ-ferrite induced from solid-state inertia welding across WAZ were further examined utilizing TEM/BF imaging. TEM analyses were conducted on the TEM thin foil specimen from four locations, interface layer, 200-400 um, 600 um and 2.0mm (i.e. base alloy) distances from the weld interface.

i) Base metal (2mm from weld-interface)

The forged austenite base alloy exhibited typical microstructural characteristics of forged metals, i.e. within a large high angle grain, there are multiple elongated subgrains with extremely high density of tangled dislocation networks (Fig. 15a-d). The areas of dark-contrast represent areas of high strain energy induced from dense dislocation network (Fig. 15b).

δ-ferrite phase was not obvious in these TEM/BF images of the forged base alloy. It could be present in areas outside the small thin TEM sample or the particle(s) were too small, <<1.0um, to be visible in the highly strained matrix.
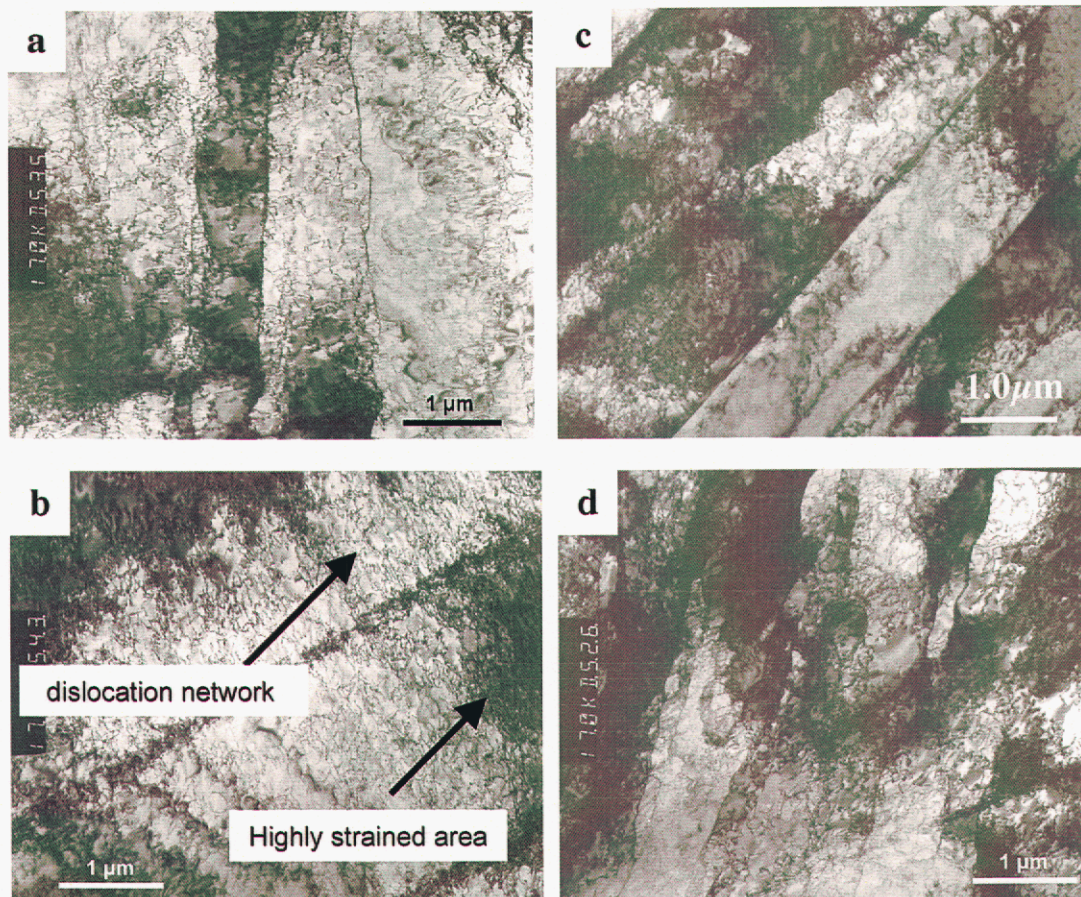

Figure 15: TEM/BF images of the heavily deformed subgrains in the forged base alloy. a-d) microstructure of four different areas in the TEM thin foil specimen.

ii) Interface layer

Austenite grains in the interface are relatively small 2-5um. Highly strained subgrains were absent. The fine austenite grains contained moderate untangled dislocations that are substantially lower in density than those seen in the base alloy (Fig.16 a-b). The low dislocation density in the austenite matrix is suggestive of low angle recovered grains or high angle recrystalized grains. It is suspected that the majority of the austenite grains seen in the interface layer were recrystallized. This conclusion was based on the large difference in diffracting contrast among the adjacent austenite grains seen by SEM/BEI (Fig. 10, 13 and 14) implying significant misorientation, typical of recrystallization

Regarding δ-ferrite transformation, TEM/BF images also show lace-like δ-ferrite along grain boundaries of the fine austenitic grains. The ferrite laces are $\leq$ 2.0um wide and decorate the fine-grained austenite boundaries semi-continuously (Fig. 16c-d). They did not appear to inherit the fragmented stringer-type morphology frequently seen in the forged base alloy.
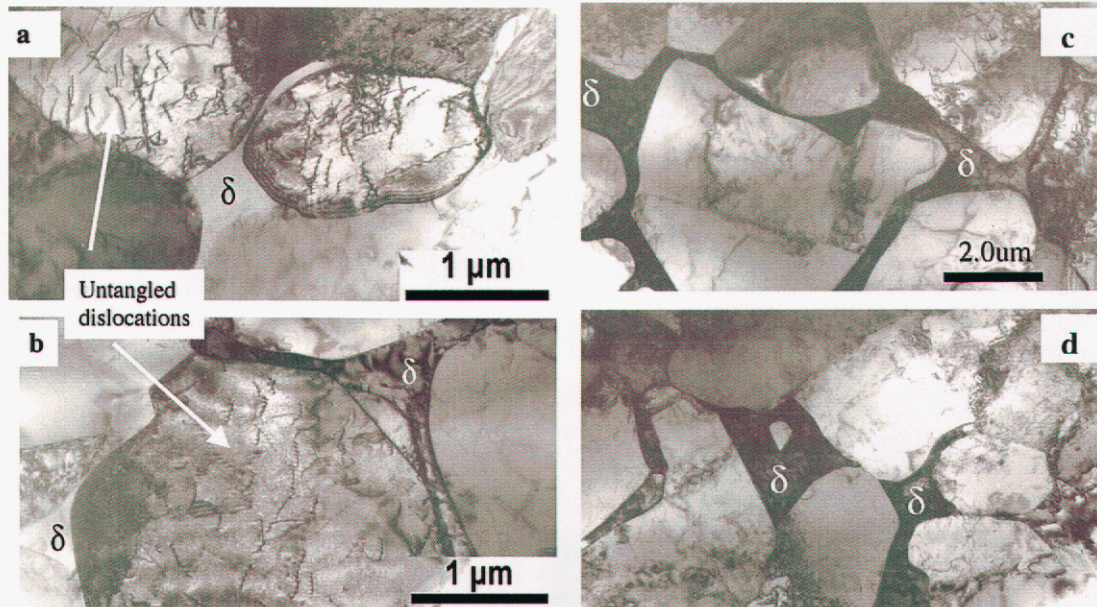

Figure 16): a-b) TEM/BF images showing low density of untangled dislocation in fine-grained austenite matrix at the interface.

Figure 16: c-d) TEM/BF images showing lace-like δ-ferrites formed along grain boundaries of fine-grained austenite matrix.

26

Chemical composition of the phases was analyzed using TEM/EDS. The EDS spectra in Figure 17 display typical elemental composition of δ-ferrite and austenite matrix in the interface layer and the base alloy. Visually, the X-ray peak intensity ratio of Cr to Fe is different between the δ-ferrite and austenite matrix. Cr to Fe ratio in the δ-ferrite appeared to be slightly higher than those in the austenite matrix. Quantitative TEM/EDS analyses show Cr is ~6wt% higher and Ni is ~ 3.0wt% lower in δ-ferrite than those in the adjacent austenite matrix (Table 3). It is noted that chemical composition of austenite at the interface and in base alloy are comparable which is suggestive of absence of massive elemental diffusion. Ni concentration in the base alloy, is ~2wt% higher than the nominal composition of the 21-6-9 alloy. The source of the elevated Ni is being examined.
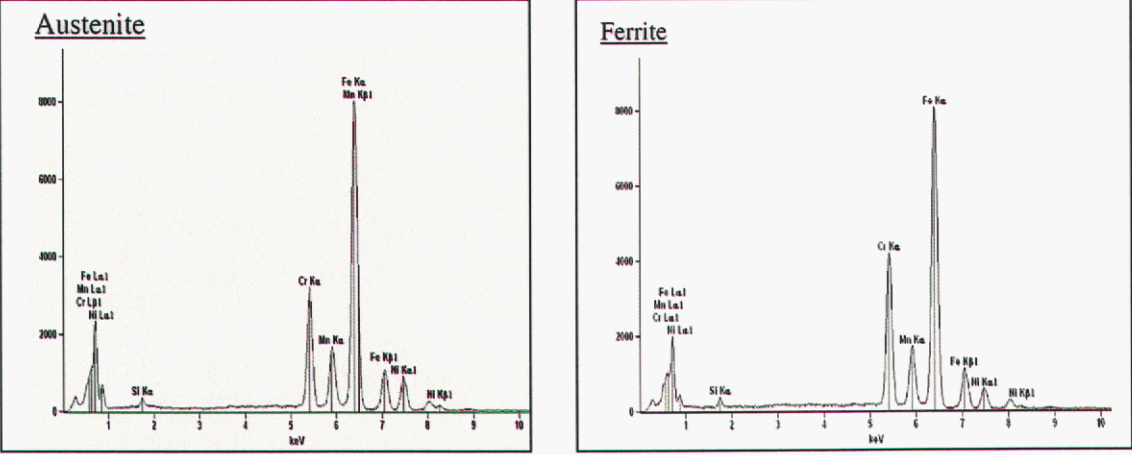
Figure 17: TEM/EDS spectra showing typical chemical composition of ferrite and austenite in the interface layer. Elemental composition was quantified as listed in Table 2.

Table 2: Chemical composition (wt%)				
	Austenite at interface wt%	Ferrite at interface wt%	Austenite base metal wt%	Composition of 21-6-9 forging wt%
Cr	21.05	27.32	21.02	19.6
Mn	9.02	8.16	9.07	9.3
Fe	62.96	60.37	61.82	63.5
Ni	6.97	4.16	8.09	6.7
N				0.27
Si				0.61

iii) Intermediary Layer, 200-400 um from the weld-interface

Austenite matrix grains in this layer in general were much coarser (Fig. 18b). However, There are still some fine-grain remnants present in this layer (Fig. 18a). Highly deformed subgrains were also absent in the austenite matrix. Austenite matrix grains contained low density of untangled dislocations similar to those found in the interface layer, (Fig. 18a-b). δ-ferrite phase was not observed in this coarse-grained layer. Average grain size of austenite was not measured from the TEM images due to the limited sampling area.
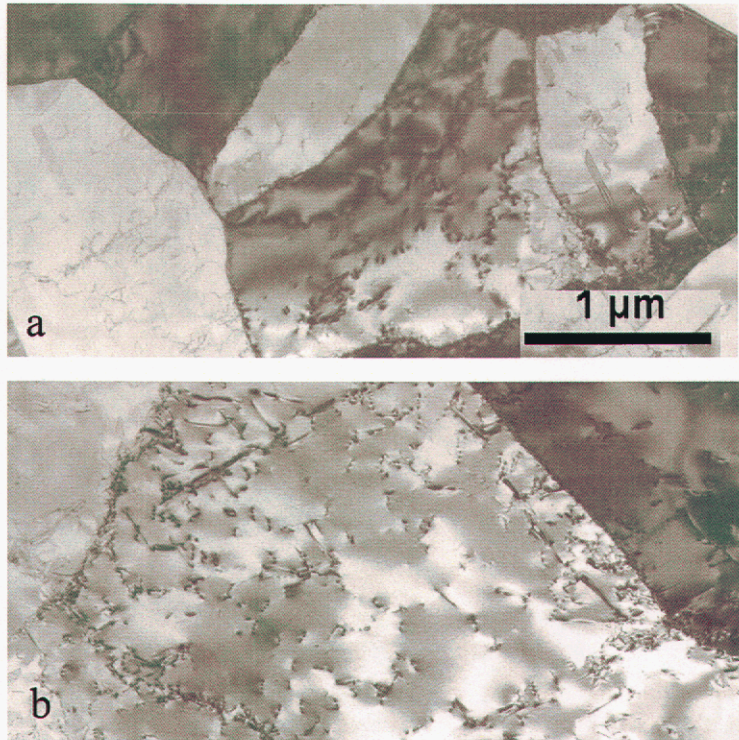
Figure 18: TEM/BF images showing low density of Untangled dislocation in the intermediary layer.

Summary and Discussion

Current studies have identified two major metallurgical characteristics, i.e. recrystallization and δ-ferrite transformation, of the 21-6-9 inertia welds. Overall microstructure evolution and austenite-ferrite transformation across WAZ are illustrated by the TEM/BF images shown in Figure 19. The images show absence of highly strained subgrains in the weld affected zone (WAZ) (Fig. 19a-e) and presence of lace-like δ-ferrite in the interface layer along the fine-grained austenite matrix (Fig. 19a-b). It is believed that the major portion of WAZ was recrystallized. The recrystallization was concluded based on absence of subgrains, low density of untangled dislocations (Fig.20) and large difference in diffracting contrast among the adjacent grains. In addition, we suspect that δ-ferrite transformation took place at the highly deformed weld interface during welding. This conclusion was reached based on the δ-ferrite's chemical identity and its unique morphology, i.e. semi-continuous laces decorating boundaries of those newly crystallized fine austenite grains.
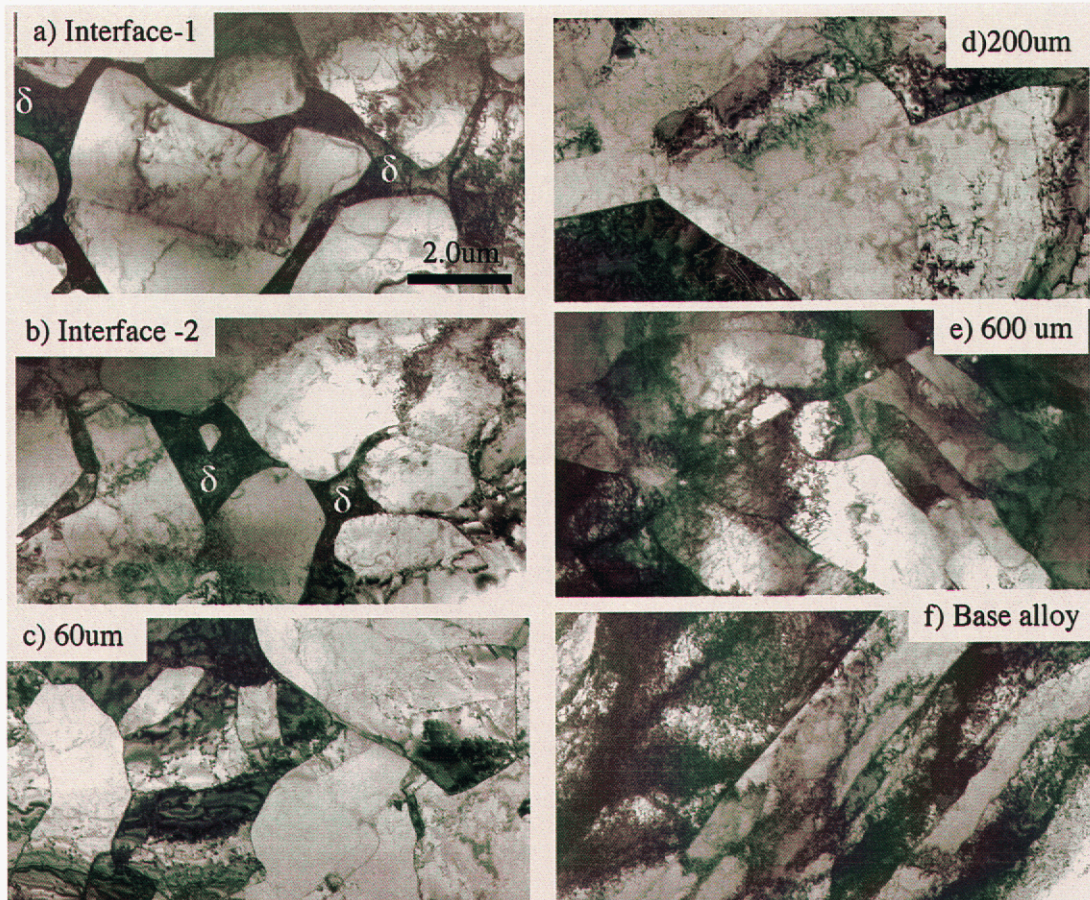

Figure 19: TEM/BF images showing density of dislocation networks decrease with distance from the interface. A-b) Interface layer contained fine grains and low dislocation density, c-d) Intermediary layer, 200-400um from interface, contained coarse grain and low dislocation density, e-f) At 600um and beyond from interface contained fine subgrains and dense dislocation networks
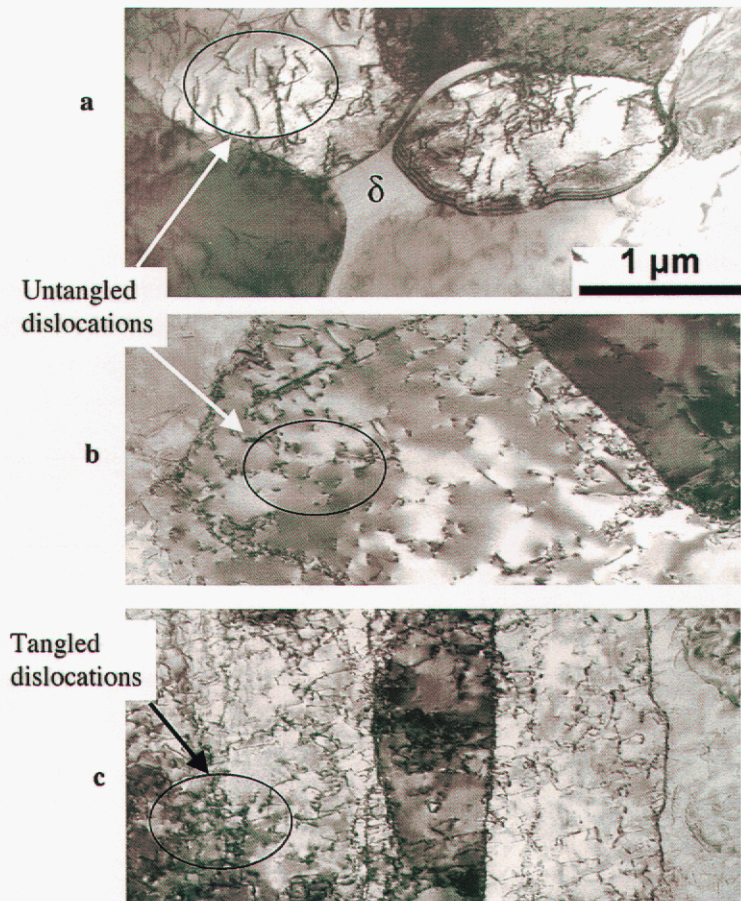
Figure 20: TEM/BF showing density of dislocation network, a-b) low density untangled dislocations in the interface and intermediate layer respectively, c) dense tangled dislocation network in the forged base alloy.

Current results suggest both recrystallization and δ-ferrite formation are attributed to combined factors of thermal heating and plastic deformation induced during inertia welding. The following discussion contains additional observations and some scientific rationale supporting the conclusions made concerning the recrystallization and δ-ferrite phase transformation of IW welds.

Recrystallization

Nonlinear recrystallized microstructural features across the WAZ suggest additional factor(s) besides localized heating affect local nucleation and grain growth. In a GTA weld, thermal heating is the major factor; therefore, recrystallization is dictated by the thermal history, i.e. time and temperature. Consequently, grain size variation in a GTA weld is dictated by a monotonic thermal distribution, which does not describe either the history or structure observed in the current inertia welds.

A possible explanation of the fine-grained austenite strands seen in the interface layer is that they were derived from combinations of 1) high number of nucleation sites supplied from constant generation of dense dislocation networks and 2) pinning of grain boundaries from fine-ferrite particles generated during welding. Fragmented strands of bimodal austenite grain structures in the interface may be the result of repetitive cycles of nucleation and grain growth from continuing unidirectional mechanical deformation.

The transition zone (or intermediary layer) between the interface layer and base alloy is dictated by a complex and nonlinear interaction of strain rate and temperature. These combinations produce critical conditions for recrystallization and grain growth. Grain coarsening next to the interface is suspected to be dominated by thermal heating. At long distance, 200-400um, from the joint, the dislocation density is expected to be substantially lower than in the interface zone resulting in low number of nucleation sites, and therefore coarser recrystallized grains.

δ-ferrite transformation

The key findings concerning δ-ferrite transformation in the interface layer are:

- δ-Ferrite was detected primarily along the weld-interface layer where the alloy was subjected to the most severe deformation, i.e. contained the highest density of dislocation network.
- Lace-like δ-ferrite present mainly along the newly recrystallized fine-grained austenite and was absent in the coarse-grained regions. In addition, the ferrite did not inherit the stringer-type morphology of the pre-existing ferrite from the base alloy.
- δ-ferrite contained higher Cr and lower Ni than the adjacent austenite matrix implying elemental diffusion occurred locally.

The above findings imply the transformation possibly was promoted by localized Cr and Ni diffusion due to combination of thermal heating and continuous plastic deformation.

The overall argument is that assuming localized thermal distribution alone affecting the metallurgy in the interface layer, one should not expect a bimodal austenite grain size and should see more homogenous δ-ferrite distribution, contrary to what was observed. From this inconsistency, we infer that the microstructure evolution in the WAZ is the result of a highly non-linear combination of temperature and plastic strain.

Other potential factors, which might influence elemental diffusion and subsequently influence δ-ferrite transformation, are being investigated such as local melting of small areas of 30-50um sizes in the interface layer and/or localized chemical segregation derived from the macrosegregation banding seen in the forging precursors.

Intentionally Left Blank

Conclusions

- Major metallurgical features found in the current inertia welds are recrystallization of the weld-affected zone (WAZ) and δ-ferrite transformation at the interface.
- Recrystallization was responsible for softening in the WAZ, which averaged about 20% lower hardness than the base alloy.
- Heterogeneous nucleation and grain growth seen across the WAZ resulted in nonuniform hardness profile in the welds. This nonlinear recrystallization most likely was caused by different combined factors of thermal heating and plastic strain resulting in a variable dislocation density during welding.
- Grain refinement at the highly deformed interface is a result of high number of nucleation sites supplied from dense dislocation network coupling possibly with pinning of grain boundaries by fine δ-ferrite particles.
- A potential influence from other factors such as banded elemental macrosegregation of forging precursors on the elemental diffusion is being examined.

Intentionally Left Blank

Future work

Joint research efforts by current authors and the staff in 8772 are underway to study kinetics and metallurgy and their relationship to welding variables and performance. The current experimental activities engaged by the current author include:

- Design a test matrix for assessing the effect of welding variables as shown in the following table.
- Additional microstructure characterization for the welds produced by various groups supported by the IW welding development program.
- Design mechanical testing methods for evaluating bond strength and fracture toughness of the welds relevant to this program.

Table 3

The following feed stock forging material has been allocated and will be welded with the current established inertia weld parameters at SNL,CA.

Material	Ferrite number of bar stock	Approximate yield strength of forging (ksi)	Expected number of welds
21-6-9 MCN 112761	~2	100	4
21-6-9 MCN 200687	~0	100	4
22-13-5 heat no. 534861	~0	120	4
22-13-5 heat no. 534861	~0	100	4

These materials were identified based on the need to understand the effects of composition on microstructures in inertial welded material, namely the role of ferrite in 21-6-9 and the role of strength in 22-13-5.

Intentionally Left Blank

Acknowledgement

References

(1)   JA Brooks, SH Goods, CV Robinson. Weld Properties of a Free Machining Stainless Steel. SAND2000-8002.

(2)   M. Preuss, J.W.L. Pang, P.J. Withers, G.L. Baxter. Metall Mater Trans 33A (2002) 3215-3225.

Intentionally Left Blank

Distribution

Intentionally Left Blank

40